Journal of Solid State Chemistry 315 (2022) 123469

Contents lists available at ScienceDirect

Journal of Solid State Chemistry

journal homepage: www.elsevier.com/locate/jssc

Why is Mn charge ordered and AFM coupled in $YBaMn_2O_5$?

Pavel Karen

Department of Chemistry, University of Oslo, Blindern, N-0315, Oslo, Norway

ARTICLE INFO

Keywords:
Liquid-mixing synthesis
Charge order
A-site ordered double perovskite

ABSTRACT

Synthesis conditions to obtain single-phase $YBaMn_2O_5$ are reported and its crystal structure refined from neutron powder diffraction data collected between 25 and 600 °C in the paramagnetic state. The structure parameters are used to reason why the phase maintains ordered ionic charges of Mn instead of mixing them at an elevated temperature, why this Mn^{2+} and Mn^{3+} ordering is of the checkerboard type in all three dimensions, and why these ions would couple antiferromagnetic upon cooling.

1. Introduction

The three solid phases of the A-site ordered double perovskite along the $YBaMn_2O_{5-5.5-6}$ line convert one to another via reversible oxygen absorption at moderate temperatures, and this wide composition span opens for applications as oxygen-scavenger or -storage materials, solid-oxide fuel-cell cathodes, or as catalytic oxidants [1]. The $YBaMn^{II}Mn^{III}O_5$ end phase [2] of Mn^{2+} and Mn^{3+} configurations d^5 and d^4 is one-step from d^4 and d^3 of $LaCaMn^{III}Mn^{IV}O_6$ [3] and other colossal-magnetoresistance perovskite manganites [4,5]. It is also one-step from d^6 and d^5 that leads to valence mixing in $YBaFe^{II}Fe^{III}O_5$ [6] above the Verwey-type [7] transition temperature.

There are notable differences between the Fe and Mn variants. While the d_{xz} orbital order in $YBaFe_2O_5$ stabilizes charge ordering that defies the electrostatic minimum for *point* charges by alternating chains of Fe^{2+} coordinations and chains of Fe^{3+} coordinations [6], the Mn^{2+} and Mn^{3+} in $YBaMn_2O_5$ comply with it and alternate in all three directions [8]. While iron atoms in $YBaFe^{II}Fe^{III}O_5$ become equivalent above 335 K [6], $YBaMn^{II}Mn^{III}O_5$ remains charge ordered even at 873 K, as observed in the neutron diffraction study [9] of $TbBaMn_2O_5$ in an equilibrium 1:1 mixture with $TbBaMn_2O_{5.5}$. Only the magnetic cooperative order is the same, as charge-ordered $YBaFe_2O_5$ [6], and somewhat surprisingly $YBaMn_2O_5$ at low temperatures [8], both adopt the G-type spin arrangement of Wollan–Koehler [3]. $YBaFe_2O_5$ does so with moments along *b*, $YBaMn_2O_5$ along *c*.

In this study, synthesis conditions to obtain phase-pure $YBaMn^{II}Mn^{III}O_5$ of non-magnetic and redox-stable yttrium were established, and the crystal structure investigated by high-intensity neutron powder diffraction up to 873 K for signs of approaching valence mixing. The refined structure parameters are used to calculate molecular-orbital energies, from which it is argued how the magnetic ordering in $YBaMn_2O_5$ complies with the Goodenough's model [10] for semicovalent exchange and what it might take to mix the Mn valences.

2. Experimental

Syntheses and characterizations. Polycrystalline $YBaMn_2O_{5+w}$ was sintered from precursors obtained by liquid mixing in melted citric acid monohydrate [11]. Annealed Y_2O_3 (99.99%, Fluka) was dry-mixed with the citric acid (BDH AnalaR reagent, <0.01% sulfated ash, <0.002% Ca), in amount of 2 mol per mole of cation charge of each starting component, and dissolved upon melting assisted by water added just to cover the bottom of the beaker. Manganese lumps (99.9%, Ventron) were cleaned of oxide in a 1:1 diluted hydrochloric acid, washed, and dried. The obtained 8.3786 g of Mn was dissolved in 50 mL water upon gradual additions of in total 80 mL of 65% HNO_3 and then added dropwise into the above melt to a complete release of nitrous gasses. After cooling below 100 °C, redistilled water was added on top of the viscous melt, and barium carbonate (Fluka, <0.2% Sr) was dissolved upon warming. The resulting clear melt of brown color was decomposed in a drying oven at 180 °C into an organic-based solid xerogel, which spontaneously incinerated overnight (unexpected, see typical synthesis details in Ref. [12]). The product was milled, pressed into cylindrical pellets of 15 mm in diameter and calcined for 24 h at 860 °C in a flowing atmosphere of 10.01(2) mole % H_2 in Ar (AGA, certified analysis) wetted in a saturated solution of KBr at 18 °C. The water-formation equilibrium then fixes the oxygen partial pressure in the reaction atmosphere to $\log(p_{O2}/\text{bar}) \approx -18.5$. Because small amounts of Y_2O_3 were detected in the calcination product, a second calcination was performed on the rehomogenized sample under flowing atmosphere of the above-used 10% H_2/Ar gas mixed with Ar (AGA, 6 N purity) to an Ar/H_2 molar ratio of 78(3) and wetted at 19 °C to stabilize $\log(p_{O2}/\text{bar}) \approx -16.6$. This yielded a pure mixture of the $YBaMn_2O_5$-type and $YBaMn_2O_{5.5}$-type phases of brown color. After testing the optimal sintering conditions (Table 1), pellets of 8 mm in diameter were pressed at 150 bar and sintered for 24 h at 1200 °C into a silvery $YBaMn_2O_{5.006}$ under flowing atmosphere of 10% H_2/Ar gas mixed with Ar in two steps and wetted in the saturated solution of KBr at

https://doi.org/10.1016/j.jssc.2022.123469
Received 15 July 2022; Accepted 1 August 2022
Available online 11 August 2022

Table 1
Sintering conditions that led to single-phase $YBaMn_2O_{5+w}$ samples.

w *	t/°C	Ar/H_2 **	log(p_{O2}/bar)	porosity
0.016	1000	1940(37)	−10.98(2)	60%
0.010	1100	2246(118)	−9.36(6)	37%
−0.003	1200	2277(155)	−8.09(5)	5.7%
0.006	1200	2551(48)	−7.94(2)	5.6%

* Standard deviations are less than ±1 unit of the last decimal.
** Volume ratio; standard deviations refer to gas-mixing variations over time.

21.8 °C (details in Table 1). A phase-pure product was obtained upon free cooling inside the furnace in the flowing atmosphere, the wetting of which was switched off below 1000 °C in order to exclude oxygen that would be needed to oxidize this large and highly sintered sample. Powder-diffraction checks were performed with a D5000 diffractometer and $CuK_{\alpha 1}$ radiation.

Wet chemical analyses of oxygen content. The oxygen content in $YBaMn_2O_{5+w}$ was determined iodometrically. A finely powdered sample of about 0.15 g and 0.8 g KI were weighed into a 10 mL glass ampoule, 5 mL H_2O was added and the ampoule was flushed by Ar. After adding 4 mL of concentrated hydrochloric acid, the ampoule was immediately sealed. The digestion of the samples lasted less than a minute when aided by heating at the bottom of the ampoule. The formed triiodide solutions were titrated under argon atmosphere with a 0.1 M thiosulfate solution of concentration standardized on KIO_3 of standard-substance quality (Merck). Close to the equivalence point, soluble starch was added as the indicator. Blank analyses were performed in order to correct for the small amount of iodine produced in the acidic environment employed for the digestion process.

Neutron powder diffraction (NPD). Data were collected at 25, 100, 200, 300, 400, 500 and 600 °C in the cryofurnace of the D2B instrument at the Institut Laue–Langevin, Grenoble, France. The two-axis diffractometer was equipped with 128 position-sensitive ^{3}He counters, and the Ge monochromator was in orientation *hkl* 335. The wavelength $\lambda = 1.59421$ Å was standardized on CeO_2. Coarsely powdered $YBaMn_2O_{5.006}$ (~10 g) was sealed in a vanadium container under He atmosphere. The primary collimation was removed from the setup in order to achieve higher intensity at the expense of resolution. The slit was set to 100/100 so that the beam size at the sample was 2 × 5 cm^2. The counting limit was 1.6×10^5 counts per step of 0.05° of the angle 2θ. The angular range was 5–160° (2θ).

Rietveld refinements. Crystal-structure refinements in the GSAS software suite [13] used the Chebyshev function of 18 parameters to model the background. The NPD peak profiles were fitted by Simpson integration of the Thompson–Cox–Hastings pseudo-Voigt profile with two Gaussian and one Lorentzian profile parameters refined together with the zero point, transparency and asymmetry.

Orbital energy calculations. The molecular-orbital energy levels for isolated manganese–oxygen coordinations were calculated from structural data with the CAESAR 2.0 (Crystal And Electronic Structure AnalyzeR) software package [14]. The basis-set coefficients for this Extended-Hückel tight-binding method were listed previously [6].

3. Results and discussion

The synthesis conditions of the highly sintered $YBaMn_2O_{5.006(0)}$ NPD sample of ~10 g are listed in Table 1. The iodometric titration is well reproducible, and standard deviations of the oxygen content at the fourth decimal are not unusual. The non-stoichiometry span of the synthesis tests in Table 1 is close to the formation limits of this $YBaMn_2O_5$-type structure as a single phase under given synthesis conditions, also in agreement with results in Ref. [15]. The window in terms of p_{O2} in the reaction atmosphere is narrow. As an example, at the highest temperature tested, 1200 °C, increasing the Ar/H_2 mixing ratio to 9600 in the synthesis gas wetted at 22.8 °C yielded a solid solution $YBaMn_2O_{5.67}$, the lower composition limit of which is the $YBaMn_2O_{5.5}$ reported in Ref. [9] to coexist in equilibrium with $YBaMn_2O_5$.

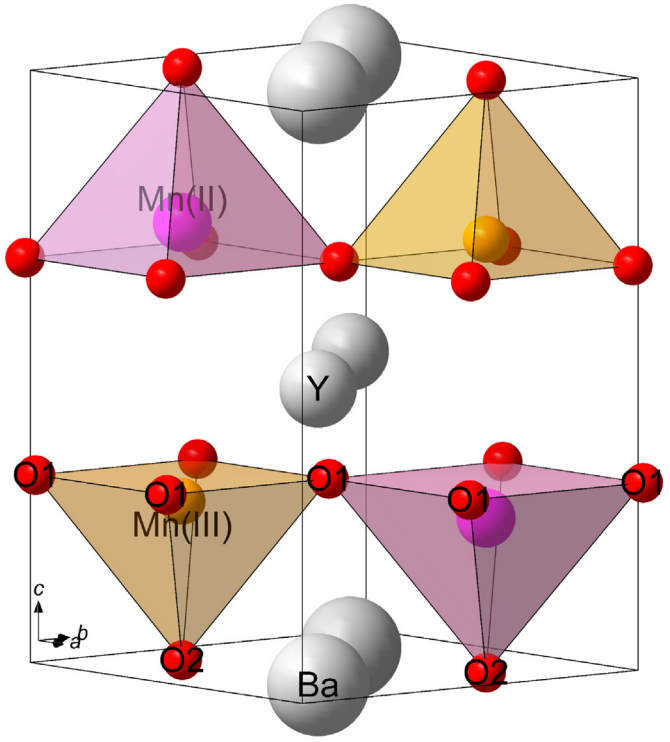

Fig. 1. *P4/nmm* unit cell of the paramagnetic $YBaMn_2O_5$ at 298 K.

The crystal structure of $YBaMn_2O_{5.006}$ was refined in the space-group *P4/nmm*, suggested in Ref. [8] for the three-dimensional checkerboard order of Mn^{2+} and Mn^{3+} (Fig. 1). The minute amount of non-stoichiometric oxygen is located in the yttrium layer between the bases of the square pyramids, and refinements of its occupancy yielded values between 0.008 and 0.014, in good agreement with the 0.006 oxygen per formula obtained by chemical analysis after the sample synthesis. The refinement shows that the crystal structure keeps the *P4/nmm* space-group symmetry within the temperature range investigated, as did $TbBaMn_2O_5$ in the NPD study of the two-phase sample in Ref. [9]. Numerical overview of the structural evolution, with refinement statistics and the refined unit cell and atomic parameters is in Table 2.

Fig. 2 illustrates the practically linear and continuous thermal expansion of this structure on unit-cell parameters per single-perovskite subcell. This suggests absence of structural or spin-state transitions in the investigated range of temperatures.

Fig. 3 shows thermal evolution of apical and basal Mn–O bond distances in the two different Mn coordination square pyramids. Whereas the four equal basal Mn–O distances are the shortest bonds in the small pyramid of d^4 Mn^{3+} (a d_{z^2}-stabilizing Jahn–Teller distortion), they are longest in the large pyramid of d^5 Mn^{2+} (a $d_{x^2-y^2}$-stabilizing Jahn–Teller distortion), and make an alternating pattern of small and large squares on the *ab* plane. All basal bonds expand linearly with temperature. The two ionic charges clearly remain ordered at all temperatures investigated.

The thermal evolution of the apical Mn–O bond lengths is less straightforward. At low temperatures, the smaller Mn^{3+} pyramid has its apical bond expanded so much by the d^4 Jahn–Teller distortion stabilizing the highest-occupied molecular orbital (HOMO) d_{z^2} as less antibonding, that it is longer than the apical distance in the adjacent larger Mn^{2+} pyramid. Fig. 1 illustrates that this is achieved by having Mn^{3+} much closer to the base of its pyramid than Mn^{2+} is to its base. Upon increasing temperature, the length difference of these two apical bonds decreases (Fig. 3). This thermally induced decrease in the d^4 Jahn–Teller distortion was also observed in other Mn^{3+} compounds such as

Table 2
Temperature evolution of the $YBaMn_2O_5$ structure parameters* and refinement figures of merit.

T (K)	298	373	473	573	673	773	873
R_{wp}	0.046	0.045	0.043	0.044	0.043	0.043	0.045
R_p	0.035	0.034	0.033	0.034	0.033	0.033	0.035
R_F^2	0.033	0.038	0.041	0.049	0.054	0.058	0.070
χ^2	3.258	3.162	3.002	3.094	3.083	3.153	3.461
a (Å)	5.54891(8)	5.55306(8)	5.55801(8)	5.56386(8)	5.56928(4)	5.57506(9)	5.58125(9)
c (Å)	7.65836(13)	7.67326(13)	7.68955(12)	7.70642(13)	7.72131(13)	7.73706(13)	7.75332(13)
V (Å^3)	235.80(10)	236.62(10)	237.54(10)	238.56(10)	239.49(10)	240.48(10)	241.52(11)
z Mn^{2+}	0.74624(54)	0.74571(54)	0.74429(55)	0.74384(58)	0.74445(61)	0.74590(61)	0.74641(68)
z Mn^{3+}	0.27565(53)	0.27493(52)	0.27458(54)	0.27413(58)	0.27360(63)	0.27398(65)	0.27379(74)
x_{O1}	0.49138(18)	0.49135(18)	0.49163(19)	0.49174(20)	0.49227(23)	0.49235(25)	0.49287(31)
z_{O1}	0.31668(10)	0.31670(10)	0.31677(10)	0.31679(11)	0.31653(11)	0.31678(12)	0.31676(13)
z_{O2}	0.00724(58)	0.00833(55)	0.00950(53)	0.00988(57)	0.00983(62)	0.00910(67)	0.00841(79)
O3 occ.	0.008(4)	0.014(4)	0.010(4)	0.010(4)	0.009(4)	0.008(4)	0.012(4)

* Space group *P4/nmm* number 129 and origin choice 2, Wyckoff positions: Y 2*b*, Ba 2*a*, Mn^{2+} 2*c*, Mn^{3+} 2*c*, O1 8*j*, O2 2*c*, O3 2*c* of *z* fixed to ½ and occupancy (occ.) refined. Observed reflections: 166, refined variables: 39.

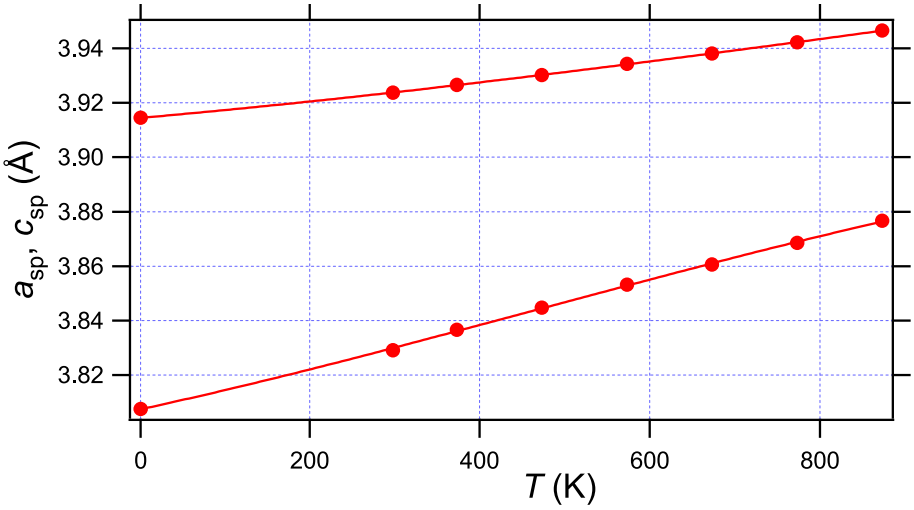

Fig. 2. Thermal evolution of the unit-cell parameters per single-perovskite subcell. The values for 1.5 K are from Ref. [8].

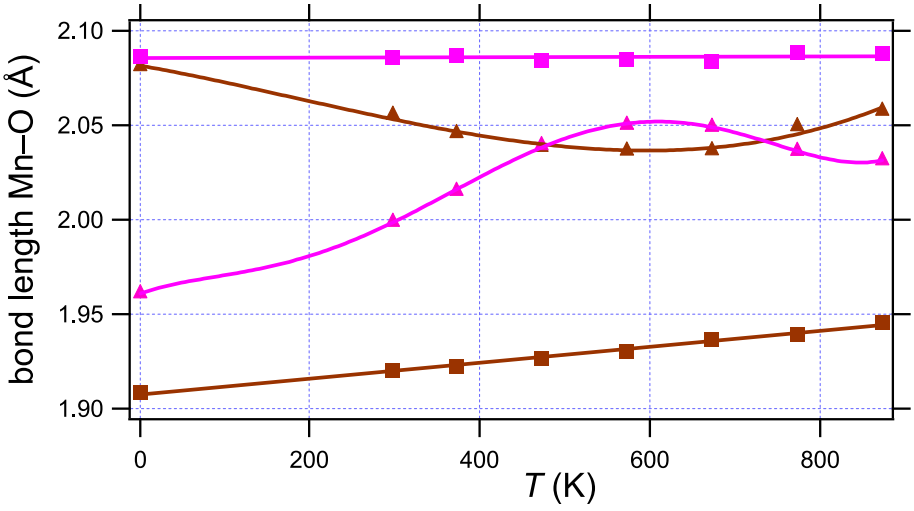

Fig. 3. Thermal evolutions of bond lengths Mn^{2+}–O (magenta) and Mn^{3+}–O (brown) to the square-pyramidal basis (■) and to the apex (▲). The 1.5 K values are from Ref. [8]. Lines are guides for eye.

stoichiometric $LaMnO_3$, where it disappears at about 750 K [16,17]. In $YBaMn_2O_5$, the apical and basal Mn–O distances in each pyramid become closest at about 600 K (Fig. 3) due to this thermal alleviation of the Jahn–Teller distortion. From that point up, a slow mutual approach of the two Mn valences starts, demonstrated by resumed contraction of the apical distance in the larger Mn^{2+} pyramid versus expansion in the smaller Mn^{3+} one, both upon the overall thermal expansion.

Fig. 4 shows the evolution of the bond-valence sums (BVS) of the two

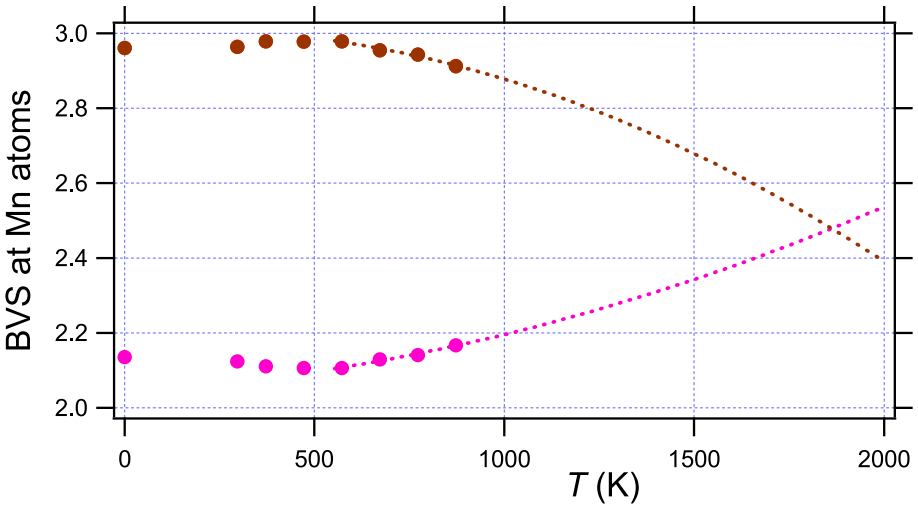

Fig. 4. Thermal evolution of the bond-valence sums (BVS) at the two crystallographically different Mn atoms. The BVS for 1.5 K is calculated from data in Ref. [8].

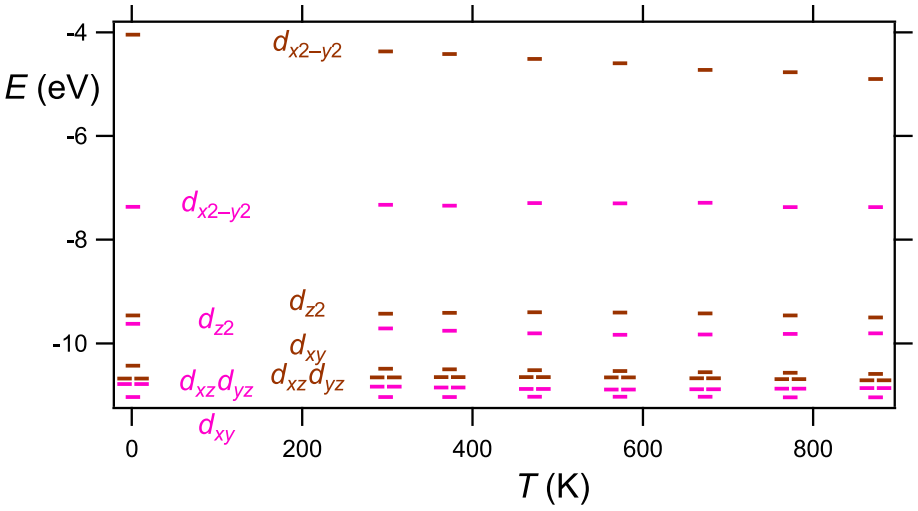

Fig. 5. Evolution of energies of essentially nonbonding Mn orbitals calculated for $(Mn^{3+}O_5)^{7-}$ (brown) and $(Mn^{2+}O_5)^{8-}$ (magenta). Orbital symbols refer to local coordinate systems centered at Mn and oriented in the direction of the O atoms. The energies for 1.5 K are calculated from atomic coordinates in Ref. [8].

manganese atoms, calculated with the average Mn–O single-bond length 1.75 Å according to Ref. [18]. As expected, the BVS values are close to +2 and +3, and they do start a mutual approach around 600 K. Extrapolation of the four highest-temperature points in Fig. 4 gives an upper estimate for how far $YBaMn_2O_5$ may be from valence mixing.

The energies of the essentially nonbonding orbitals of the $YBaMn_2O_5$ high-spin [2,8] cations Mn^{2+} and Mn^{3+} in their ligand field were calculated with CAESAR 2.0 and are plotted in Fig. 5 as a function of temperature. In the small Mn^{3+} coordination pyramid, the Jahn–Teller expansion of the apical bond upon contraction of basal bonds destabilizes the empty $d_{x^2-y^2}$ orbital by as much as 4.9 eV from d_{z^2} at 300 K, and that makes the Mn^{3+} d^4 configuration behave as a *half*-filled orbital set. The apical oxide anion then mediates an antiferromagnetic semicovalent superexchange [10] with the truly *half*-filled spin-polarized orbital set of Mn^{2+} d^5 (Fig. 6). This is what yields below T_N = 167 K [8,19] the observed [8] G-type [3] coupling of all manganese spins. The basal oxygens of the pyramids mediate likewise. Their buckling angle Mn^{2+}–O–Mn^{3+} in $YBaMn_2O_5$ (157.20(10)° at 298 K versus 156.75(14) at 873 K) is the same as in the charge-ordered phases $YBaFe_2O_5$ of 158.59(31)° at 20 K [6] or $YBaCo_2O_5$ of 156.30(88)° at 50 K [20], where the G-type coupling was identified by NPD in their charge-ordered state (on $HoBaFe_2O_5$ [21] and $HoBaCo_2O_5$ [22]). Also DFT calculations [23, 24] confirm the $YBaMn_2O_5$ G-type spin order. Only $YBaMn_2O_5$ turns into a ferrimagnet upon cooling, though, since its checkerboard charge order coincides with the G-type spin order, which makes all Mn^{2+} moments to point up (along *c* [8]) and all Mn^{3+} down.

Valence mixing via sharing the excess electron of Mn^{2+} by both manganese atoms that face each other in Fig. 1 would have to be accomplished via their d_{z^2} orbitals, as in $YBaFe_2O_5$ [25]. Fig. 6 illustrates how much the energies of the d_{z^2} orbital (in blue) for the electron of fixed spin orientation differ between Mn^{2+} and Mn^{3+}. In contrast, in the charge-ordered $YBaFe_2O_5$ of Fig. 7, the minority-spin Fe^{2+} electron has only 0.8 eV to the Fe^{2+} d_{z^2} orbital that is 0.2 eV below the d_{z^2} of Fe^{3+} to mix with and thus couple these two Fe ferromagnetic (blue arrow) by this electron sharing across the Y layer [6].

4. Conclusions

Synthesis conditions to obtain single-phase $YBaMn^{II}Mn^{III}O_5$ by sintering at high-temperatures make a narrow window of oxygen partial pressures in the reaction atmosphere (Table 1). Likewise narrow is the range in temperatures. Whereas sintering at 1000 °C yields porosity of 60%, the silvery product at 1200 °C has 6%. The crystal structure in the paramagnetic state, refined from neutron powder diffraction data

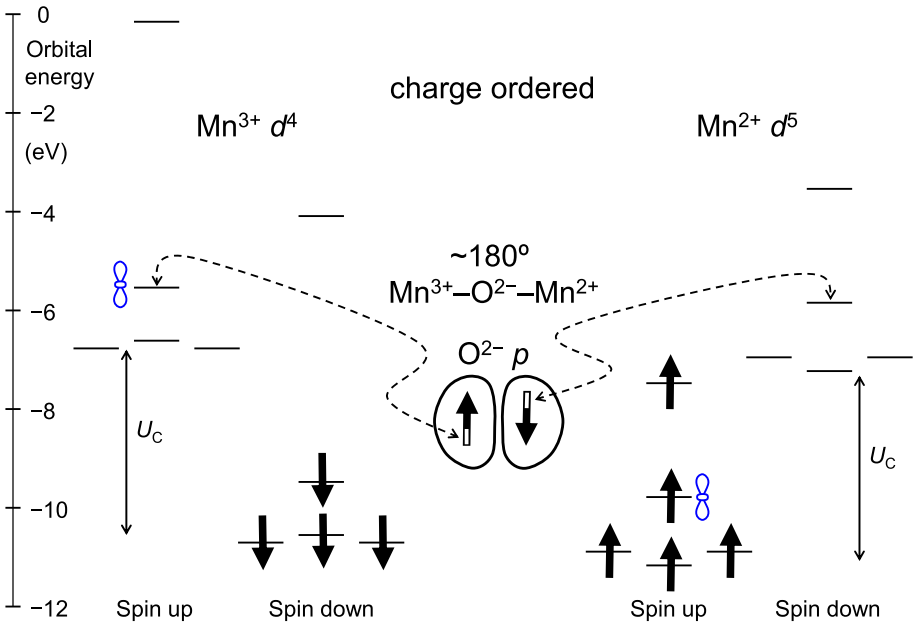

Fig. 6. Charge-ordered $YBaMn_2O_5$. Semicovalent linear superexchange interaction of effectively half-filled d^4 Mn^{3+} and half-filled d^5 Mn^{2+} cations. The spin-pairing energy U_C is drawn to permit the observed [8] Mn^{2+} high-spin state. The two d_{z^2} orbitals to eventually share the valence-mixing electron at high temperature are marked in blue.

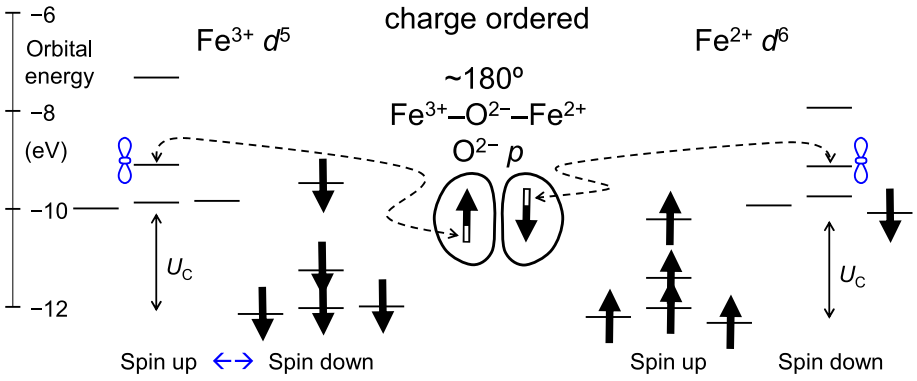

Fig. 7. Charge-ordered $YBaFe_2O_5$ on the scale of Fig. 6. Semicovalent linear superexchange interaction of half-filled d^5 Fe^{3+} and of d^6 Fe^{2+} cations. The spin-pairing energy U_C is drawn to permit the observed [6] Fe^{2+} high-spin state. In blue: Upon demise of the charge ordering, the minority-spin Fe^{2+} electron in the ordered d_{xz} orbital will mix via d_{z^2} orbitals (blue shapes) of the two Fe atoms facing each other across their pyramidal bases and couple them ferromagnetic (blue double arrow) in the still antiferromagnetic crystal [6].

collected between 25 and 600 °C, maintains Mn^{2+} and Mn^{3+} ordered in a three-dimensional checkerboard pattern of electrostatic minimization; a pattern that in $YBaFe_2O_5$ is modified by orbital ordering [6].

At ambient temperature, the presence of one electron in the Mn^{3+} HOMO d_{z^2} expands the apical Mn–O distance of this small coordination pyramid due to Jahn–Teller distortion. The apical distance of the larger Mn^{2+} square pyramid is contracted due to corresponding expansion of its basal Mn–O distances that stabilizes the Mn^{2+} HOMO $d_{x^2-y^2}$. Upon warming to ~600 K, the apical and basal Mn–O distances become closest both in the larger Mn^{2+} and in the smaller Mn^{3+} pyramid (Fig. 3), due to thermal alleviation of the Jahn–Teller distortion. Above this temperature, the Mn^{2+}–O apical distance begins to contract and Mn^{3+}–O expand upon the overall thermal expansion. From this point, the BVS at Mn^{2+} and Mn^{3+} start slowly approaching one another as a first sign of a possible valence mixing at a higher temperature.

Extended-Hückel calculations of the orbital energies for the isolated square-pyramidal coordinations around Mn^{3+} and Mn^{2+} bring further details. The very high energy of the Mn^{3+} LUMO $d_{x^2-y^2}$ makes this electron configuration effectively half-filled. The semicovalent superexchange interaction [10] of such d^4 Mn^{3+} and d^5 Mn^{2+} half-filled electron configurations via the intervening oxygen then yields antiferromagnetic coupling of the two unequal-spin manganese atoms. Furthermore, the calculations show that the energies of the d_{z^2} electron of the same spin orientation differ profoundly between Mn^{2+} and Mn^{3+}, and this is what makes it hard to mix thermally the Mn^{2+} excess electron with Mn^{3+} in $YBaMn_2O_5$ when compared with the easy mixing in $YBaFe_2O_5$.

Interestingly, combining Mn and Co in the prototype double-cell perovskite structure does not simulate $YBaFe_2O_5$. There is no charge ordering, no valence mixing, just a Co^{2+} and Mn^{3+} solid solution of d^7–d^4 configurations [26]. The reason is redox chemistry. If the product were $YBaCo^{III}Mn^{II}O_5$, the Co^{3+} and Mn^{2+} d^6–d^5 configuration would have behaved as it does in $YBaFe^{II}Fe^{III}O_5$.

CRediT authorship contribution statement

Pavel Karen: Conceptualization, Data curation, Formal analysis, Investigation, Methodology, Project administration, Resources, Software, Validation, Visualization, Writing – original draft, Writing – review & editing.

Declaration of competing interest

The authors declare that they have no known competing financial interests or personal relationships that could have appeared to influence the work reported in this paper.

Data availability

Data will be made available on request.

Acknowledgements

The author acknowledges the Institut Laue–Langevin for provision of neutron radiation facilities and thanks Dr. Emmanuelle Suard for assistance in using the two-axis D2B diffractometer in 2005.

Appendix A. Supplementary data

Supplementary data to this article can be found online at https://doi.org/10.1016/j.jssc.2022.123469.

References

[1] T. Motohashi, T. Ueda, Y. Masubuchi, M. Takiguchi, T. Setoyama, K. Oshima, S. Kikkawa, Remarkable oxygen intake/release capability of $BaYMn_2O_{5+\delta}$: applications to oxygen storage technologies, Chem. Mater. 22 (2010) 3192–3196, https://doi.org/10.1021/cm100290b.

[2] J.P. Chapman, J.P. Attfield, M. Molgg, C.M. Friend, T.P. Beales, A ferrimagnetic manganese oxide with a layered perovskite structure: $YBaMn_2O_5$, Angew. Chem., Int. Ed. 35 (1996), https://doi.org/10.1002/anie.199624821, 2482–1384.

[3] E.O. Wollan, W.C. Koehler, Neutron-diffraction study of the magnetic properties of the series of perovskite-type compounds $La_{1-x}Ca_xMnO_3$, Phys. Rev. 100 (1955) 545–563, https://doi.org/10.1103/PhysRev.100.545.

[4] G.Q. Gong, C.L. Canedy, G. Xia, J.Z. Sun, A. Gupta, W.J. Gallagher, Colossal magnetoresistance in the antiferromagnetic $La_{0.5}Ca_{0.5}MnO_3$ system, J. Appl. Phys. 79 (1996) 4538–4540, https://doi.org/10.1063/1.362564.

[5] L.M. Rodríguez-Martínez, J.P. Attfield, Cation disorder and size effects in magnetoresistive manganese oxide perovskites, Phys. Rev. B 54 (1996) R15622–R15625, https://doi.org/10.1103/PhysRevB.54.R15622.

[6] P.M. Woodward, P. Karen, Mixed valence in $YBaFe_2O_5$, Inorg. Chem. 42 (2003) 1121–1129, https://doi.org/10.1021/ic026022z.

[7] E.J.W. Verwey, Electronic conduction of magnetite (Fe_3O_4) and its transition point at low temperatures, Nature 144 (1939) 327–328, https://doi.org/10.1038/144327b0.

[8] F. Millange, E. Suard, V. Caignaert, B. Raveau, $YBaMn_2O_5$: crystal and magnetic structure reinvestigation, Mater. Res. Bull. 34 (1999) 1–9, https://doi.org/10.1016/S0025-5408(98)00214-1.

[9] E. Castillo-Martinez, A.J. Williams, J.P. Attfield, High-temperature neutron diffraction study of the cation ordered perovskites $TbBaMn_2O_{5+x}$ and $TbBaMn_2O_{5.5-y}$, J. Solid State Chem. 179 (2006) 3505–3510, https://doi.org/10.1016/j.jssc.2006.07.019.

[10] J.B. Goodenough, Theory of the role of covalence in the perovskite-type manganites $[La,M^{(II)}]MnO_3$, Phys. Rev. 100 (1955) 564–573, https://doi.org/10.1103/PhysRev.100.564.

[11] P. Karen, A. Kjekshus, Citrate-gel syntheses in the Y(O)—Ba(O)—Cu(O) system, J. Am. Ceram. Soc. 77 (1994) 547–552, https://doi.org/10.1111/j.1151-2916.1994.tb07028.x.

[12] P. Karen, Synthesis and equilibrium oxygen nonstoichiometry of $PrBaFe_2O_{5+w}$, J. Solid State Chem. 299 (2021), 122147, https://doi.org/10.1016/j.jssc.2021.122147.

[13] A.C. Larson, R.B. Von Dreele, General Structure Analysis System (GSAS), Los Alamos National Laboratory Report, 2000. LAUR 86-748.

[14] J. Ren, W. Liang, M.H. Whangbo, Crystal and Electronic Structure Analysis Using CAESAR, PrimeColor Software, Inc., Cary NC, 1998.

[15] K. Jeamjumnunja, W. Gong, T. Makarenko, A.J. Jacobson, A determination of the oxygen non-stoichiometry of the oxygen storage material $YBaMn_2O_{5+\delta}$, J. Solid State Chem. 230 (2015) 397–403, https://doi.org/10.1016/j.jssc.2015.07.044.

[16] A.K. Bogush, V.L. Pavlov, L.V. Balyko, Structural phase transitions in the $LaMnO_{3+\lambda}$ system, Cryst. Res. Technol. 18 (1983) 589–598, https://doi.org/10.1002/crat.2170180504.

[17] J. Rodriguez-Carvajal, M. Hennion, F. Moussa, A.H. Moudden, L. Pinsard, A. Revcolevschi, Neutron-diffraction study of the Jahn–Teller transition in stoichiometric $LaMnO_3$, Phys. Rev. B 57 (1998) R3189–R3192, https://doi.org/10.1103/PhysRevB.57.R3189.

[18] M. O'Keeffe, N.E. Brese, Atom sizes and bond lengths in molecules and crystals, J. Am. Chem. Soc. 113 (1991) 3226–3229, https://doi.org/10.1021/ja00009a002.

[19] J.A. McAllister, J.P. Attfield, A variable temperature neutron diffraction study of the layered perovskite $YBaMn_2O_5$, J. Mater. Chem. 8 (1998) 1291–1294, https://doi.org/10.1039/A800605I.

[20] T. Vogt, P.M. Woodward, P. Karen, B.A. Hunter, P. Henning, A.R. Moodenbaugh, Low to high spin-state transition induced by charge ordering in antiferromagnetic $YBaCo_2O_5$, Phys. Rev. Lett. 84 (2000) 2969–2972, https://doi.org/10.1103/PhysRevLett.84.2969.

[21] P.M. Woodward, E. Suard, P. Karen, Structural tuning of charge, orbital and spin ordering in double-cell perovskite series between $NdBaFe_2O_5$ and $HoBaFe_2O_5$, J. Am. Chem. Soc. 125 (2003) 8889–8899, https://doi.org/10.1021/ja034813+.

[22] E. Suard, F. Fauth, V. Caignaert, I. Mirebeau, G. Baldinozzi, Charge ordering in the layered Co-based perovskite $HoBaCo_2O_5$, Phys. Rev. B 61 (2000), R11871, https://doi.org/10.1103/PhysRevB.61.R11871 (R).

[23] R. Vidya, P. Ravindran, P. Vajeeston, H. Fjellvåg, A. Kjekshus, Spin, charge, and orbital orderings in oxides with dual-valent transition metal ions, Ceram. Int. 30 (2004), https://doi.org/10.1016/j.ceramint.2003.12.198, 1993–1998.

[24] H.P. Xiang, X.J. Liu, Z.J. Wu, J. Meng, Influence of Mn–O–Mn bond angle on the magnetic and electronic properties in $YBaMn_2O_5$, J. Phys. Chem. B 110 (2006) 2606–2610, https://doi.org/10.1021/jp054386h.

[25] J. Lindén, F. Lindroos, P. Karen, Orbital occupancy evolution across spin- and charge-ordering transitions in $YBaFe_2O_5$, J. Solid State Chem. 252 (2017) 119–128, https://doi.org/10.1016/j.jssc.2017.04.036.

[26] P. Karen, E. Suard, F. Fauth, P.M. Woodward, $YBaMnCoO_5$; neither valence mixed nor charge ordered, Solid State Sci. 6 (2004) 1195–1204, https://doi.org/10.1016/j.solidstatesciences.2004.06.010.